RSC Advances

PAPER

Solvothermal synthesis and luminescence properties of BaCeF$_5$, and BaCeF$_5$:Tb^{3+} nanocrystals

Tianqi Sheng,[ab] Zuoling Fu,*[ab] Jing Wang,[ab] Xihong Fu,[d] Yingning Yu,[c] Shihong Zhou,[c] Siyuan Zhang[c] and Zhenwen Dai*[ab]

Cubic monodisperse BaCeF$_5$ and BaCeF$_5$:Tb^{3+} nanocrystals have been successfully synthesized by a citric acid assisted solvothermal method. The crystalline phase, size, morphology, and luminescence properties were characterized using powder X-ray diffraction (XRD), field emission-scanning electron microscopy (FE-SEM), transmission electron microscopy (TEM), photoluminescence (PL), photoluminescent excitation spectra (PLE) as well as dynamics decay. The results reveal that the Tb^{3+}-doped BaCeF$_5$ sample shows a strong green emission centered at 546 nm, corresponding to the $^5D_4 \rightarrow ^7F_5$ transition of Tb^{3+} due to an efficient energy transfer from Ce^{3+} to Tb^{3+}. The decay lifetime of Ce^{3+} monotonically increases with increase of Tb^{3+} concentration. The critical energy transfer distance between Ce^{3+} and Tb^{3+} was also calculated by methods of concentration quenching and spectral overlapping. Experimental analysis and theoretical calculations reveal that the dipole–dipole interaction should be the dominant mechanism for the Ce^{3+}–Tb^{3+} energy transfer.

1. Introduction

Over the past few decades, the study of nanometric luminescent materials, especially lanthanide ion-doped luminescent nanomaterials, has become one of the hottest topics in nanoscience because of their potential applications in high performance magnets, luminescent devices, catalysts, and other functional materials arising from 4f electrons.[1–5] As an important group of inorganic materials with unique optical and electronic properties, nano and submicroscale fluoride materials have drawn increasing attention. For example, the syntheses of metal fluoride nanomaterials, such as CaF$_2$ nanocubes,[6,7] SrF$_2$ nanospheres,[8] and BaF$_2$ nanocubes[9] and nanorods[10] have been reported for their application in UV lithography, UV-transparent optical lenses, and surface conditioning of glass. Besides, binary lanthanide fluorides (LnF$_3$, Ln = lanthanide elements)[11–14] and ternary ALnF$_4$ (A = alkali metals, Ln = lanthanide elements)[15–22] fluorides were intensively researched with potential applications in display, laser, and biological labels in recent years. Compared with the fluorides mentioned above, alkaline-earth lanthanide ternary fluorides have obtained relatively little attention. Barium yttrium fluoride crystals such as BaY$_2$F$_8$ and BaYF$_5$ are prepared[19] as excellent host matrixes that can be doped with divalent and trivalent lanthanide ions, exhibiting the strong broadband emission in the near UV spectra region (360–440 nm)[23] and highly efficient infrared-to-visible up-conversion light.[24] However, the lanthanide ions doped BaCeF$_5$ system has never reported up to now.

In general, alkaline-earth lanthanide ternary fluorides, for examples, bulk BaLn$_2$F$_8$/BaYF$_5$ crystals[25,26] and nonstoichiometric single crystals R$_{1−y}$M$_y$F$_{3−y}$ (R = La–Er; M = Ca, Sr, Ba, Cd)[27] were prepared by traditional solid-state reaction method. Due to insufficient mixing and low reactivity of raw materials, several impurity phases easily co-exist in the product. Therefore, in recent years, several wet chemical techniques such as co-precipitation method,[28] hydrothermal method,[29–31] liquid-solid-solution procedure[32,33] and solvothermal method[34] were used to prepare the fluorides phosphor. Phosphor materials synthesized by these wet chemical methods have many advantages, *i.e.*, high purity, homogenous composition and fine grains in the nanometer range. To the best of our knowledge, there has been no literature available on the wet chemical synthesis of cubic-phase BaCeF$_5$, so we have undertaken this work. In this paper, we realize the solvothermal synthesis of BaCeF$_5$, and BaCeF$_5$:Tb^{3+} nanocrystals and research the luminescence properties of Ce^{3+} and Tb^{3+} in cubic BaCeF$_5$. Moreover, the energy transfer efficiency from Ce^{3+} to Tb^{3+}, the energy transfer critical distance (R_c) between Ce^{3+} and Tb^{3+}, and the energy transfer mechanism of Ce^{3+}–Tb^{3+} in BaCe$_{1−x}$Tb$_x$F$_5$ nanocrystals have been discussed in detail.

[a] State Key Laboratory of Superhard Materials, College of Physics, Jilin University, Changchun, 130012, China. E-mail: zlfu@jlu.edu.cn (Z. Fu); dai@jlu.edu.cn (Z. Dai); Fax: 86-431-85167966; Tel: 86-431-85167966
[b] Key Lab of Coherent Light, Atomic and Molecular Spectroscopy, Ministry of Education, Changchun, 130012, China
[c] State Key Laboratory of Rare Earth Resources Utilization, Changchun Institute of Applied Chemistry, Chinese Academy of Sciences, Changchun, 130022, China
[d] Changchun Institute of Optics, Fine Mechanics and Physics, Chinese Academy of Sciences, Changchun, 130033, China

2. Experimental

2.1. Synthesis of the samples

Materials. The samples were synthesized through a citric acid assisted solvothermal method. The raw materials $BaCO_3$ (99.0%), $Tb(NO_3)_3 \cdot 6H_2O$ (99.99%), $Ce(NO_3)_3 \cdot 6H_2O$ (99.99%), NH_4F (99.99%) and $C_6H_8O_7 \cdot H_2O$ (99.5+%) were all purchased from Sinopharm Chemical Reagent Co. Ltd. and were used directly, without further purification.

Synthesis. In a typical procedure of preparing $BaCeF_5$ nanocrystals, the first mixture: 2 mmol of $Ce(NO_3)_3 \cdot 6H_2O$ was first added into 20 mL of isopropyl alcohol with stirring to form a transparent homogeneous solution. Subsequently, the second mixture: 20 mL of isopropyl alcohol containing 48 mmol of NH_4F (1.776 g), 2 mmol of $BaCO_3$ (0.39468 g) and 2 mmol of $C_6H_8O_7 \cdot H_2O$ (0.42028 g) were added into the above solution with stirring to form a transparent homogeneous solution. After the addition of the second mixture into the first mixture, the end mixture became white and turbid. After stirring for about 60 min, the resultant solution was transferred into a 60 mL Teflon autoclave. Finally, the autoclave was sealed and heated at 180 °C for 12 h followed by cooling to the room temperature naturally. The resulting precipitates were washed with deionized water and ethanol each two times. The final product was dried at 60 °C for 12 h in air. Then, in a typical procedure of preparing $BaCeF_5$: (2 mol%) Tb^{3+} nanocrystals, the first mixture: 1.96 mmol of $Ce(NO_3)_3 \cdot 6H_2O$ and 0.04 mmol of $Tb(NO_3)_3 \cdot 6H_2O$ were first added into 20 mL of isopropyl alcohol with stirring to form a transparent homogeneous solution. The next steps were the same as the preparation of $BaCeF_5$ nanocrystals. Finally, we can obtain $BaCeF_5$: (2 mol%) Tb^{3+} nanocrystals. Similarly, other $BaCe_{1-x}Tb_xF_5$ (x = 0.04,0.06,0.08,0.10,0.12) samples are synthesized by the same process.

2.2. Characterization

The structural characteristics of the final products were examined by the powder X-ray diffraction (XRD) pattern using Cu-Kα (λ = 0.15405 nm) radiation on a Rigaku-Dmax 2500 diffractometer. The morphology and the size of the obtained samples were observed with field emission-scanning electron microscopy (FE-SEM, JSM-6700F, JEOL) and transmission electron microscopy (TEM, JEM-2010 JEOL). The ultraviolet-visible photoluminescence excitation and emission spectra were recorded with a Hitachi F-7000 spectrophotometer equipped with Xe-lamp as an excitation source. All the measurements were performed at room temperature.

3. Results and discussion

3.1. Crystal structure and morphologies

Fig. 1 presents representative XRD patterns of $BaCe_{1-x}Tb_xF_5$ samples with different concentrations. The powder XRD data of the as-synthesized product shows nine characteristic diffraction peaks (25.61°, 29.67°, 42.50°, 50.28°, 52.69°, 61.61°, 67.81°, 69.81°, 77.62°) in 2θ range of 10° to 80°. Compared with the cubic structure $BaCeF_5$ (JCPDS # 43-0394, space group Fm-$3m$[225], cell parameters $a = b = c = 6.018$ Å), the absence

of some diffraction peaks implies that the crystal structure of the as-synthesized product may have a higher symmetry in the space group. No impurity lines are observed in the patterns of the Tb^{3+} doped nanocrystals shown in Fig. 1(b)–(h), meaning that the RE^{3+} doping does not cause any significant changes in the crystal phases. In addition, it is worth noting that the diffraction peaks are widened as a result of the small-size effect of the nanocrystals. The mean crystallite size of the product was estimated from the XRD pattern according to the Scherrer formula $D = K\lambda/\beta\cos\theta$, where λ is the X-ray wavelength (0.15406 nm), β is the full-width at half-maximum, θ is the diffraction angle, and K is a constant (0.89). The estimated mean crystallite size is 38.05 nm.

A representative panoramic FE-SEM image shown in Fig. 2(a) demonstrates that the product is composed of well dispersed particles with small sizes. The high-magnified TEM image (Fig. 2(b)) further shows the nanocrystals more distinctly. Most of the nanocrystals are pseudospherical particles with a mean size of about 40 nm, which is in consistent with the size estimated by Scherrer formula from the XRD pattern. The selected-area electron diffraction (SAED) in Fig. 2(c) exhibits dots, which are due to the diffraction of ensemble nanocrystals, indicating that the as-obtained nanocrystals are essentially single crystalline in nature. The interplanar distance obtained from the dot is 0.3475 nm, which can be assigned to (111) lattice planes of cubic structure $BaCeF_5$, respectively. In Fig. 2(d) the interplanar distance is 0.3475 nm, which is also matched with the (111) plane.

3.2. Luminescence properties

Fig. 3(a) shows the photoluminescence excitation (λ_{em} = 344 nm) and photoluminescence emission (λ_{ex} = 292 nm) spectra of the $BaCeF_5$ nanocrystals. The excitation spectrum of the $BaCeF_5$ nanocrystals gives a broadband centered at 292 nm with a shoulder centered at 270 nm, which were attributed to the electric dipole-allowed transitions of the Ce^{3+} ions from the 4f shell to the 5d orbital. Owing to the influences of crystal field splitting and spin–orbit coupling, the 4f→5d transition of the Ce^{3+} ions will exhibit a subtle structure.[35] Under excitation at 292 nm, the emission spectrum of $BaCeF_5$ nanocrystals exhibits an intense
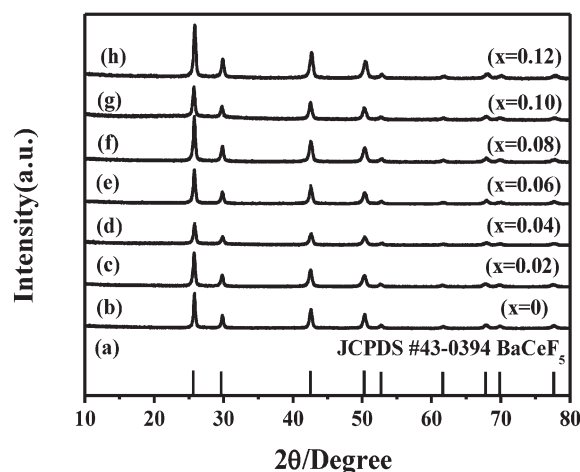
Fig. 1 XRD patterns of samples $BaCe_{1-x}Tb_xF_5$ and reference date JCPDS#43-0394.
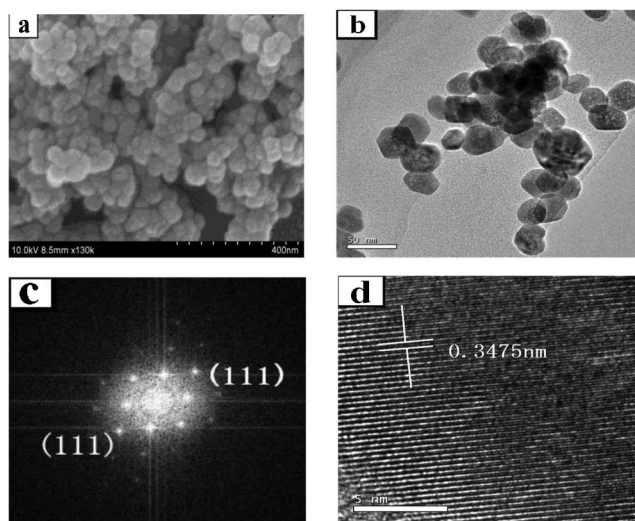
Fig. 2 (a) FE-SEM image of $BaCe_{0.90}Tb_{0.10}F_5$ sample. (b) TEM image of the sample. (c) SAED pattern of the particle. (d) HRTEM image of the sample.

ultraviolet emission band centered at 344 nm, which is assigned to the 5d–4f electronic transition of the Ce^{3+} ions. Fig. 3(b) shows the photoluminescence excitation (λ_{em} = 546 nm) spectrum of the $BaCe_{0.98}Tb_{0.02}F_5$ nanocrystals and photoluminescence emission (λ_{ex} = 292 nm) spectrum of the $BaCeF_5$ nanocrystals. The photoluminescence excitation (λ_{em} = 546 nm) spectrum of $BaCe_{0.98}Tb_{0.02}F_5$ nanocrystals in the Fig. 3(b) are similar with the photoluminescence excitation (λ_{em} = 344 nm) spectrum of the $BaCeF_5$ nanocrystals in the Fig. 3(a). On the basis of the above photoluminescence excitation spectrum of the Tb^{3+} doped samples and photoluminescence spectrum of no Tb^{3+} doped samples, we can find that the emission band of Ce^{3+} overlaps well with the excitation band of Tb^{3+}. Therefore, it is expected that a resonance-type energy transfer from Ce^{3+} to Tb^{3+} in the Tb^{3+} doped $BaCeF_5$ nanocrystals may occur.

Fig. 4 gives the photoluminescence excitation (λ_{em} = 546 nm) and photoluminescence emission (λ_{ex} = 292 nm) spectra of the
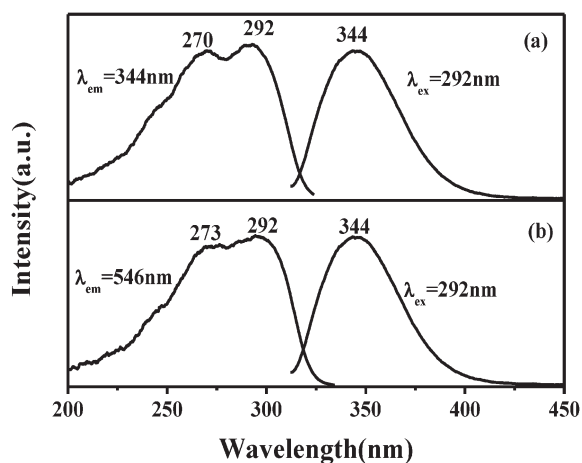
Fig. 3 (a) Excitation spectrum (λ_{em} = 344 nm) and emission spectrum (λ_{ex} = 292 nm) of $BaCeF_5$. (b) Excitation spectrum (λ_{em} = 546 nm) of $BaCe_{0.98}Tb_{0.02}F_5$ and emission spectrum (λ_{ex} = 292 nm) of $BaCeF_5$.
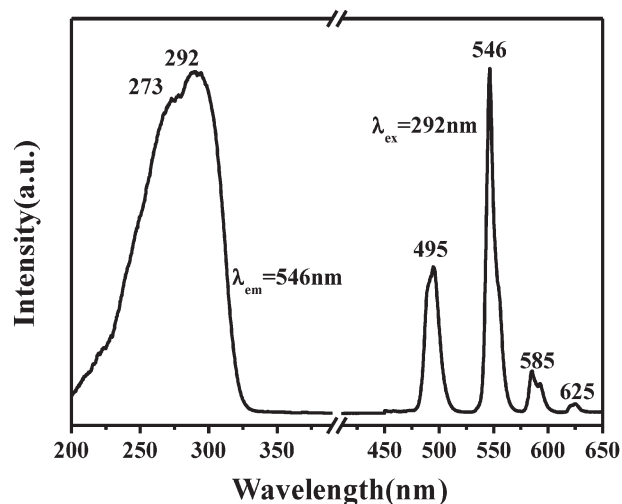
Fig. 4 Excitation (λ_{em} = 546 nm) and emission (λ_{ex} = 292 nm) spectra of $BaCe_{0.86}Tb_{0.14}F_5$.

$BaCe_{0.86}Tb_{0.14}F_5$ nanocrystals. By monitoring the 546 nm emission of Tb^{3+}, the $BaCe_{0.86}Tb_{0.14}F_5$ nanocrystal shows a broad excitation band peaking at 292 nm. With 292 nm excitation, the photoluminescence emission spectrum of $BaCe_{0.86}Tb_{0.14}F_5$ has characteristic transitions of forbidden 4f–4f transitions within the Tb^{3+} configuration in the wavelength range of 490–640 nm. The characteristic emissions of Tb^{3+} at 495, 546, 585, and 625 nm can be attributed to the transitions $^5D_4 \rightarrow {}^7F_6$, $^5D_4 \rightarrow {}^7F_5$, $^5D_4 \rightarrow {}^7F_4$, and $^5D_4 \rightarrow {}^7F_3$, respectively. The green emission ($^5D_4 \rightarrow {}^7F_5$) at 546 nm,[36] which is a magnetic dipole transition with $\Delta J = 1$, is more intense than the other transitions.[37]

To explore the possibility of the energy transfer from the Ce^{3+} to Tb^{3+} ions, Tb^{3+} ions with different concentrations were doped into the $BaCeF_5$ nanocrystals. Fig. 5 displays the emission spectra of the $BaCe_{1-x}Tb_xF_5$ nanocrystals with different Tb^{3+} concentrations, it contains both the weak emission of the Ce^{3+} ions and the strong green emission of the Tb^{3+} ions. The emission intensity of the Tb^{3+} ions gradually increases at the expense of that of the Ce^{3+} ions with the increase of Tb^{3+} doping
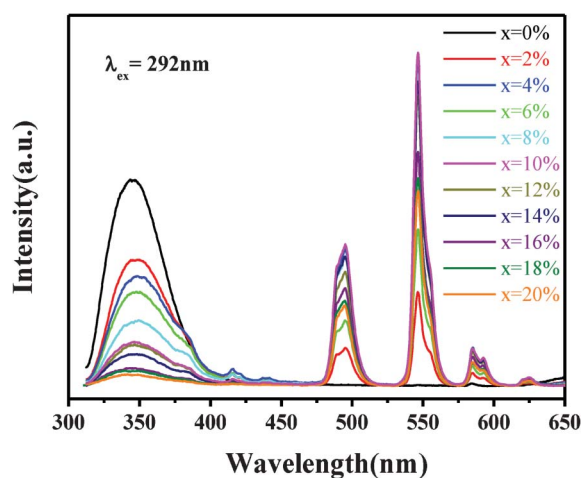
Fig. 5 Emission spectra of $BaCe_{1-x}Tb_xF_5$ (λ_{ex} = 292 nm).

concentration, indicating that the energy transfer from the Ce^{3+} to Tb^{3+} ions is highly efficient since the emission band of the Ce^{3+} ions matches well with the f–f absorptions of the Tb^{3+} ions. Until $BaCe_{0.90}Tb_{0.10}F_5$, the emission intensity of Tb^{3+} ions reaches the strongest and then the emission intensity of Tb^{3+} ions gradually decreases with the increase of Tb^{3+} doping concentration.

In order to investigate the luminescence dynamics of the samples, we measured the photoluminescence decay curves and then calculated the lifetime as well as energy transfer efficiencies. All the decay curves can be well fitted by a single exponential function as $I(t) = I_0\exp(-t/\tau)$, where I_0 is the initial emission intensity at $t = 0$, τ is the 1/e lifetime of Tb^{3+}. The lifetimes of Tb^{3+} in $BaCe_{1-x}Tb_xF_5$ samples are 2.80 ± 0.03, 2.36 ± 0.02, 2.14 ± 0.02, 1.70 ± 0.02, 1.66 ± 0.03, 1.44 ± 0.01, 1.36 ± 0.01, 1.19 ± 0.03, 1.16 ± 0.02, and 1.15 ± 0.01 ms for $x = 0.02$, 0.04, 0.06, 0.08, 0.10, 0.12, 0.14, 0.16, 0.18 and 0.20, respectively.

On the basis of the above results, Ce^{3+} acts as a sensitizer to yield sensitized luminescence from Tb^{3+} in $BaCeF_5$. A simple operational definition of energy transfer efficiency η_T in terms of lifetimes is given by:

$$\eta_T = 1 - \frac{\tau_S}{\tau_{S0}} \quad (1)$$

where τ_{S0} is the decay lifetime of Ce^{3+} in the absence of Tb^{3+} and τ_S is the lifetime of Ce^{3+} in the presence of Tb^{3+}. An alternative expression for η_T from the fluorescence yield can be expressed by the following formula:[38,39]

$$\eta_T = 1 - \frac{I_S}{I_{S0}} \quad (2)$$

where I_{S0} and I_S are the intensities of Ce^{3+} in the absence and in the presence of Tb^{3+}, respectively. The η_T from Ce^{3+} to Tb^{3+} in the $BaCe_{1-x}Tb_xF_5$ nanoparticles are calculated using eqn (2) and are illustrated in Fig. 6 as function of Tb^{3+} concentration (x). η_T equals 0, 0.157, 0.272, 0.366, 0.449, 0.522, 0.546, 0.569, 0.595, 0.605, and 0.610 for x is 0, 0.02, 0.04, 0.06, 0.08, 0.10, 0.12, 0.14, 0.16, 0.18, and 0.20, respectively. The η_T monotonically increases with the increase of Tb^{3+} concentration and is as high as 0.610 when the Tb^{3+} concentration is 0.20. It slowly changes after $x =$
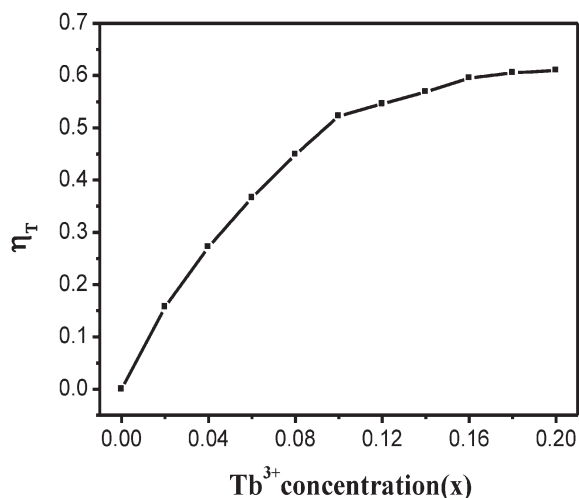
Fig. 6 Energy transfer efficiency η_T in $BaCe_{1-x}Tb_xF_5$.

0.10, indicating that the η_T has nearly reached the maximum in the sample $BaCe_{0.80}Tb_{0.20}F_5$.

According to the energy transfer theories of Dexter and Schulman, concentration quenching is due to the energy transfer from one activator to another in many cases until an energy sink in the lattice is reached.[40] We approximated the unit cell as a sphere. The volume of the sphere can be expressed as follows: $v = \frac{4}{3}\pi r^3 = \frac{V}{N}$, (where r is the radius of the sphere, N is the number of sites that a lanthanide ion can occupy per unit cell, V is the volume of the unit cell). According to the above experimental results and the crystal structure of the $BaCeF_5$ nanocrystal, we use $V = 219.2 \text{ Å}^3$, $N = 2$, and estimate the average separation $R_{Ce-Ce} = 2r = 5.94 \text{ Å}$. In Fig. 5, it has been shown that the critical concentration of C_{Tb} is 0.10. As suggested by Verstegen et al.,[41] the critical distance of the Ce^{3+}–Ce^{3+} is the critical distance of Ce^{3+}–Tb^{3+}, because the Tb^{3+} ions replace the position of the Ce^{3+} ions in the each unit cell. So in the host of $BaCeF_5$ nanocrystals, the critical concentration of C_{Tb} is 0.10 and the corresponding critical distance R_c for the Ce^{3+}–Tb^{3+} energy transfer is about 5.94 Å.

The energy transfer from a sensitizer to an activator can take place via radiative energy transfer, exchange interaction, and multipole-multipole interaction.[42] In general, the existence of radiative energy transfer from a sensitizer to an activator can be confirmed by the spectral dips in the emission spectrum of the sensitizer. The absence of the dips in the emission band of the Ce^{3+} ions corresponding to the f–f absorption lines of the Tb^{3+} ions means that the radiative energy transfer between the Ce^{3+} ions and the Tb^{3+} ions can be neglected. Moreover, the radiative energy transfer does not change the decay time of the sensitizer. The decrease of the decay time of the Ce^{3+} ions also does not support a radiative energy transfer process. Exchange interaction is strongly influenced by the distance between the sensitizer and activator and needs a large overlapping between sensitizer and activator orbitals. While both the Ce^{3+} and Tb^{3+} ions are reducing ions, such an exchange would require very high energy. Generally, the value of the critical distance is about 3–4 Å if the exchange is dominated.[43] In our case, the critical distance of Ce^{3+} and Tb^{3+} is estimated to be 5.94 Å, suggesting that energy transfer via exchange interaction can be excluded either. Thus we suspected that the energy transfer in $BaCe_{1-x}Tb_xF_5$ nanocrystals takes place via electric multipole–multipole interaction. On the basis of Dexter's energy transfer formula of multi-polar interaction and Reisfeld's approximation,[41,44,45] the following relation can be given as:

$$\frac{\eta_0}{\eta} \propto C_{Tb}^{n/3} \quad (3)$$

where η_0 and η are the luminescence quantum efficiency of the Ce^{3+} ions in the absence and in the presence of the Tb^{3+} ions, respectively; C_{Tb} is the doping concentration of the Tb^{3+} ions; and $n = 6$, 8, 10 corresponding to dipole–dipole, dipole–quadrupole, and quadrupole–quadrupole interactions, respectively. The value η_0/η can be approximately calculated by the ratio of related luminescence intensities (I_{S0}/I_S) of Ce^{3+}. The I_{S0}/I_S–$C_{Tb}^{n/3}$ plots are illustrated in Fig. 7 for $BaCe_{1-x}Tb_xF_5$. As $n = 6$, the curve exhibits the best linear relation in the three plots implying that the energy transfer from Ce^{3+} to Tb^{3+} is considered to be a dipole–dipole mechanism in the $BaCeF_5$ host.
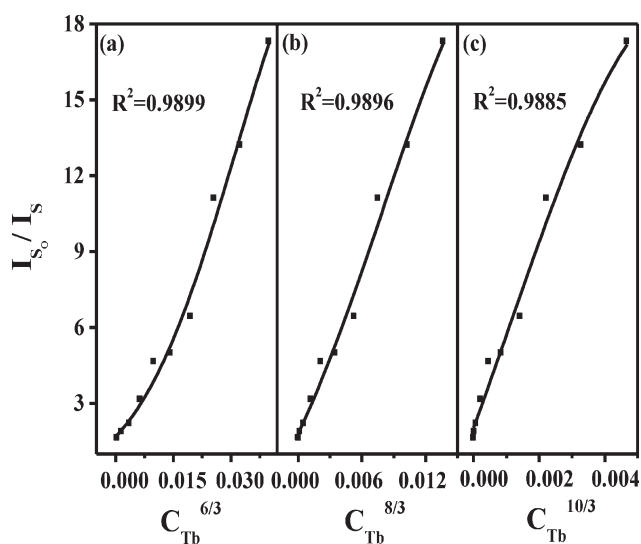
Fig. 7 Dependence of I_{S0}/I_S of Ce^{3+} on (a)$C_{Tb}^{6/3}$, (b)$C_{Tb}^{8/3}$, and (c)$C_{Tb}^{10/3}$.

According to Dexter's energy transfer theory,[45] the energy transfer process through multipolar interaction depends on the extent of overlap of the emission spectrum of the sensitizer with the absorption spectrum of the activator, the relative orientation of interacting dipoles and the distance between the sensitizer and the activator. For a dipole–dipole interaction, the energy transfer probability (P_{SA}) from a sensitizer to an activator is given by the following formula:

$$P_{SA}(dd) = \frac{3 \times 10^{12} f_d}{R^6 \tau_S} \int \frac{f_S(E) F_A(E)}{E^4} dE \qquad (4)$$

here f_d is the oscillator strength of the involved dipole absorption transition of the activator, τ_s is the radiative decay time of the sensitizer, and R is the sensitizer-activator average distance, $f_S(E)$ represents the normalized emission shape function of the sensitizer, and $F_A(E)$ is the normalized absorption shape function of the activator, and E is the energy involved in the transfer (eV).

The critical distance (R_c) of the energy transfer from the sensitizer to activator is defined as the distance for which the probability of transfer equals the probability of radiative emission of the sensitizer, i.e., the distance for which $P_{SA} \times \tau_s = 1$. Therefore, R_c can be obtained from eqn (5):

$$R_c^6 = 3 \times 10^{12} f_d \int \frac{f_S(E) F_A(E)}{E^4} dE \qquad (5)$$

The f_d of the Tb^{3+} transition is 0.3×10^{-6}.[41] Using this value and the calculated spectral overlap, the critical distance for a dipole–dipole interaction mechanism is estimated to be 5.89 Å, which little deviates from the value estimated from the critical concentration (5.94 Å), indicating that the electric dipole–dipole interaction as the main energy transfer mechanism. In addition, the dipole–dipole interaction can generally be expected to dominate in the energy transfer when both the sensitizer and the activator ions are characterized by electric dipole-allowed transitions, while the f–f transitions of Tb^{3+} are allowed by the

selection rules of electric dipole transitions. Further, the dipole–dipole interaction mechanism in the energy transfer can be determined, too. According to the above results, we believe that the energy transfer mechanism from Ce^{3+} to Tb^{3+} in the $BaCeF_5$ host should be predominated by dipole–dipole interactions.[46]

4. Conclusion

In summary, a simple solvothermal method has been used to prepare $BaCeF_5$ and $BaCeF_5:Tb^{3+}$ nanocrystals. The XRD, FE-SEM and TEM analysis indicated that the samples crystallizes in a cubic structure with spherical morphology and an average diameter of 40 nm. The photoluminescence spectra of $BaCe_{1-x}Tb_xF_5$ nanocrystals demonstrate that the energy transfer from Ce^{3+} to Tb^{3+} is highly efficient. The photoluminescence spectra of the $BaCe_{1-x}Tb_xF_5$ nanocrystals show this result, as the concentration quenching phenomenon occurs when the $x = 0.10$. The average separation between Ce^{3+} and Tb^{3+} is calculated and the critical distance R_c is 5.94 Å determined by the method of concentration quenching. The R_c calculated by spectral over-lapping method proves this. By comparison of theoretical calculation results to those of experiments, we can infer that the energy transfer from Ce^{3+} to Tb^{3+} in the nanocrystals occurs predominantly via the dipole–dipole interaction.

References

1 W. Xu, Y. Wang, X. Bai, B. Dong, Q. Liu, J. S. Chen and H. W. Song, *J. Phys. Chem. C*, 2010, **114**, 14018–14024.
2 C. X. Li and J. Lin, *J. Mater. Chem.*, 2010, **20**, 6831–6847.
3 T. Yu, J. Joo, Y. I. Park and T. Hyeon, *Angew. Chem., Int. Ed.*, 2005, **44**, 7411–7414.
4 H. X. Mai, Y. W. Zhang, R. Si, Z. G. Yan, L. D. Sun, L. P. You and C. H. Yan, *J. Am. Chem. Soc.*, 2006, **128**, 6426–6436.
5 M. Yu, H. Wang, C. K. Lin, G. Z. Li and J. Lin, *Nanotechnology*, 2006, **17**, 3245–3252.
6 X. M. Sun and Y. D. Li, *Chem. Commun.*, 2003, 1768–1769.
7 C. M. Zhang, C. X. Li, C. Peng, R. Chai, S. S. Huang, D. M. Yang, Z. Y. Cheng and J. Lin, *Chem.–Eur. J.*, 2010, **16**, 5672–5680.
8 Y. Jin, W. P. Qin and J. S. Zhang, *J. Fluorine Chem.*, 2008, **129**, 515–518.
9 P. Gao, Y. Xie and Z. Li, *Eur. J. Inorg. Chem.*, 2006, 3261–3265.
10 G. H. De, W. P. Qin, J. S. Zhang, J. S. Zhang, Y. Wang, C. Y. Cao and Y. Cui, *J. Solid State Chem.*, 2006, **179**, 955–958.
11 H. Hu, Z. G. Chen, T. Y. Cao, Q. Zhang, M. X. Yu, F. Y. Li, T. Yi and C. H. Huang, *Nanotechnology*, 2008, **19**, 375702–375712.
12 C. X. Li, J. Yang, P. P. Yang, H. Z. Lian and J. Lin, *Chem. Mater.*, 2008, **20**, 4317–4326.
13 X. L. Yang, S. G. Xiao, J. W. Ding and X. H. Yan, *J. Appl. Phys.*, 2008, **103**, 093101.
14 Z. L. Wang, Z. W. Quan, P. Y. Jia, C. K. Lin, Y. Lou, Y. Chen, J. Fang, W. Zhou, C. J. O'Connor and J. Lin, *Chem. Mater.*, 2006, **18**, 2030–2037.
15 J. L. Zhuang, J. Wang, X. F. Yang, I. D. Williams, W. Zhang, Q. Y. Zhang, Z. M. Feng, Z. M. Yang, C. L. Liang, M. M. Wu and Q. Su, *Chem. Mater.*, 2009, **21**, 160–168.

16 P. Ptacek, H. Schäfer, K. Kömpe and M. Haase, *Adv. Funct. Mater.*, 2007, **17**, 3843–3848.

17 X. Liang, X. Wang, J. Zhuang, Q. Peng and Y. D. Li, *Adv. Funct. Mater.*, 2007, **17**, 2757–2765.

18 Z. J. Wang, F. Tao, W. L. Cai, L. Z. Yao and X. G. Li, *Solid State Commun.*, 2007, **144**, 255–258.

19 Y. J. Huang, H. P. You, G. Jia, Y. H. Song, Y.H. Zheng, M. Yang, K. Liu and N. Guo, *J. Phys. Chem. C*, 2010, **114**, 18051–18058.

20 C. C. Cao, H. K. Yang, J. W. Chung, B. K. Moon, B. C. Choi, J. H. Jeong and K. H. Kim, *J. Mater. Chem.*, 2011, **21**, 10342–10347.

21 D. M. Yang, C. X. Li, G. G. Li, M. M. Shang, X. J. Kang and J. Lin, *J. Mater. Chem.*, 2011, **21**, 5923–5927.

22 D. G. Yang, X. J. Kang, M. M. Shang, G. G. Li, C. Peng, C. X. Li and J. Lin, *Nanoscale*, 2011, **3**, 2589–2595.

23 X. R. Liu, G. Xu and C. P. Richard, *J. Solid State Chem.*, 1986, **62**, 83–91.

24 L. F. Johnson, H. J. Guggenheim, T. C. Rich and F. W. Ostermayer, *J. Appl. Phys.*, 1972, **43**, 1125–1137.

25 S. Bigotta, D. Parisi, L. Bonelli, A. Toncelli and M. Tonelli, *J. Appl. Phys.*, 2006, **100**, 013109.

26 V. Toccafondo, S. A. Cerqueira and S. Faralli, *J. Appl. Phys.*, 2007, **101**, 023104.

27 N. I. Sorokin and B. P. Sobolev, *Phys. Solid State*, 2011, **50**, 416–421.

28 G. S. Yi, H. C. Lu, S. Y. Zhao, G. Yue, W. J. Yang, D. P. Chen and L. H. Guo, *Nano Lett.*, 2004, **4**, 2191–2196.

29 J. Zhuang, L. Liang, H. H. Y. Sung, X. Yang, M. Wu, I. D. Williams, S. Feng and Q. Su, *Inorg. Chem.*, 2007, **46**, 5404–5410.

30 F. Zhang, J. Li, J. Shan, L. Xu and Dm. Zhao, *Chem.–Eur. J.*, 2009, **15**, 11010–11019.

31 X. Wang and Y. Li, *Chem.–Eur. J.*, 2003, **9**, 5627–5635.

32 X. Wang, J. Zhuang, Q. Peng and Y. Li, *Inorg. Chem.*, 2006, **45**, 6661–6665.

33 S. Li, T. Xie, Q. Peng and Y. Li, *Chem.–Eur. J.*, 2009, **15**, 2512–2517.

34 H. Mai, Y. Zhang, R. Si, Z. Yan, L. Sun, L. You and C. Yan, *J. Am. Chem. Soc.*, 2006, **128**, 6426–6436.

35 H. Lai, A. Bao, Y. M. Yang, Y. C. Tao, H. Yang, Y. Zhang and L. L. Han, *J. Phys. Chem. C*, 2008, **112**, 282–286.

36 M. Yu, J. Lin, J. Fu, H. J. Zhang and Y. C. Han, *J. Mater. Chem.*, 2003, **13**, 1413–1419.

37 S. D. Cheng, C. H. Kam and S. Buddhudu, *Mater. Res. Bull.*, 2001, **36**, 1131–1137.

38 G. A. Kumar, P. R. Biju, G. Jose and N. V. Unnikrishnan, *Mater. Chem. Phys.*, 1999, **60**, 247–255.

39 P. I. Paulose, G. Jose, V. Thomas, N. V. Unnikrishnan and M. K. R. Warrier, *J. Phys. Chem. Solids*, 2003, **64**, 841–846.

40 D. L. Dexter and J. A. J. Schulman, *Chem. Phys.*, 1954, **22**, 1063–1070.

41 J. M. P. J. Verstegen, J. L. Sommerdijk and J. G. Verriet, *J. Lumin.*, 1973, **6**, 425–431.

42 G. K. Liu and B. Jacquier, *Spectroscopic Properties of Rare Earthsin Optical Materials*, Springer, Beijing, 2005.

43 B. M. Antipeuko, I. M. Bataev, V. L. Ermolaev, E. I. Lyubimov and T. A. Privalova, *Opt. Spectrosc.*, 1970, **29**, 177.

44 U. aldiño. G, *J. Phys.: Condens. Matter*, 2003, **15**, 3821–3830.

45 D. L. Dexter, *J. Chem. Phys.*, 1953, **21**, 836–850.

46 Z. Zhang, J. Wang, M. Zhang, Q. Zhang and Q. Su, *Appl. Phys. B: Lasers Opt.*, 2008, **91**, 529–537.